Surface elasticity and area incompressibility regulate fiber beading instability

A. Derya Bakiler^a, Ali Javili^b, Berkin Dortdivanlioglu^{a,c,*}

^aDepartment of Civil, Architectural and Environmental Engineering, The University of Texas at Austin, Austin, TX 78712, USA

 b Department of Mechanical Engineering, Bilkent University, 06800 Ankara, Turkey

^cOden Institute for Computational Engineering and Sciences, The University of Texas at Austin, Austin, TX 78712, USA

Abstract

A continuum body endowed with an energetic surface can exhibit different mechanical behavior than its bulk coun-

terpart. Soft polymeric cylinders under surface effects become unstable and form surface undulations referred to as

the elastic Plateau-Rayleigh (PR) instability, exclusively driven by competing surface and bulk properties. However,

the impact of surface elasticity and area compressibility, along with bulk compressibility, on the PR instability of

soft solids remains unexplored. Here we develop a theoretical, finite deformations framework to capture the onset

of the PR instability in highly deformable solids with surface tension, surface elasticity, and surface compressibility,

while retaining the compressibility of the bulk as a material parameter. In addition to the well-known elastocapillary

number, surface compressibility and a dimensionless parameter related to the surface modulus emerges that governs

the instability behavior of the structure. The results of the theoretical framework are analyzed for an exhaustive list

of bulk and surface parameters and loading scenarios, and it is found that increasing surface elasticity and surface

incompressibility preclude PR instability. Theoretical results are compared with high-fidelity numerical simulation

results from surface-enhanced isogeometric finite element analysis and an excellent agreement is observed across a

broad range of material parameters and large deformation levels. Our results demonstrate how surface effects can

be used to (i) render stable soft structures and prevent PR instability when it occurs as an unwanted by-product of

manufacturing techniques or (ii) tune the instability behavior for possible applications involving polymer fibers.

Keywords: Plateau–Rayleigh instability, surface elasticity, compressible elasticity, polymer fiber, eigenvalue analysis

1. Introduction

It is well known that the surface of a body exhibits different mechanical behavior compared to that of the encased

bulk. As size decreases and hence surface-to-volume ratio increases, the effect of the surface starts to prevail over that

of the bulk. Thus, accounting for surface effects introduces a length scale into the problem which is inherently missing

*Corresponding author.

Email address: berkin@utexas.edu (Berkin Dortdivanlioglu)

in classical continuum mechanics formulations. The length scale at which surface effects begin to dominate over bulk effects typically ranges from O(nm) for stiff materials like nanostructures, to O(nm) for soft materials like polymeric gels. This surface energy of solids is governed by surface tension, and material parameters related to stiffening and area compressibility defined through surface Lamé parameters [1]. Stiffening material surfaces which dictate the overall mechanical behavior of the structure can be seen in elastomers, e.g. via exposing the surface to UV radiation [2]. Similarly, hydrogels, which can have compressible or incompressible bulks, have been shown to form significant surface layer through shrinking [3, 4] or oxidation polymerization at mold surfaces [5]. The compressibility of the surface area can vary widely, as demonstrated by lipid bilayers whose compressibility changes with their lipid content, as shown by molecular dynamics simulations and experimental results [6]. Nearly incompressible surface behavior is often assumed for red blood cells [7]. In addition, surface properties can be modified through the application of thin film or hydrogel coatings. Finally, it is worth noting that a common surface model in the literature considers only surface tension, without stiffening effects, and has been used in numerous works referenced in this study.

The competition between surface tension and bulk elastic energy results in what is called the elastocapillary effect, which is known to deform elastic solids at small length scales and even cause the structure to become unstable. In fluids, surface tension driven motion brings forward the Plateau–Rayleigh (PR) instability resulting in a stream breaking into spherical droplets [8]; with soft solids, elastocapillary effect results in the PR-like instability with a long-wavelength cylinder-like pattern, experimentally observed in [9]. The PR instability of solids has been of increasing interest over the past few years, as it has been spotted in various biological structures such as spider silk capture threads [10, 11], nerve fibers [12] and blood vessels under high blood pressure [13], as well as presenting themselves in the fabrication of microfluidic devices [14] and as byproducts in electrospun polymer fibers [15] which are becoming increasingly popular due to their potential and economical applications in drug delivery [16] and tissue regeneration [17, 18].

The elastocapillary effect which governs the PR instability has been well established, see [4, 9] among others, wherein an "elastocapillary number" $\Gamma := \frac{\gamma}{\mu \ell}$, a dimensionless quantity which is defined as the ratio of surface tension γ to bulk shear modulus μ and radius of the fiber ℓ , has been identified as the governing parameter for the onset of the long-wave instability in soft cylindrical gels. Works have focused on pattern formation in swelling and shrinking gels, experimentally [3] and theoretically [19, 20]. The PR instability with various geometries, such as tubes [21, 22] and torus [23], material models, such as compressible neo-Hookean [24, 25] or viscoelastic [26], dielectric elastomers [27] and anisotropy [28] has been looked into, together with post-bifurcation behavior [24].

Hence, the competition between the surface effects resulting from surface stiffening and area compressibility and bulk effects, and how it influences the PR instability behavior of soft solids remains virtually unexplored. Furthermore,

almost all of these works on the solid PR instability deal with the *incompressible* material regime based on the assumption that polymers and biological matter live close to the incompressible limit. However, hydrogels have been shown to have Poisson's ratios ranging between 0.165 - 0.5 [29–31], together with recent works demonstrating that biological matter such as brain tissue [32] and human skin [33] indeed are *far from being incompressible*. Hence, the objective of this work is three-fold: (i) to develop a theoretical framework using incremental stability analysis suitable for the PR instability analysis of soft cylinders subjected surface tension, together with surface elasticity effects, (ii) conduct the said analysis in a generic, large deformation, compressible setting, and (iii) compare analytical results to numerical results obtained via surface-enhanced *isogeometric* finite element method (FEM) capable of performing eigenvalue analysis. The gaps in literature it aims to fill and the outcomes of the work are summarized briefly in Fig. 1.

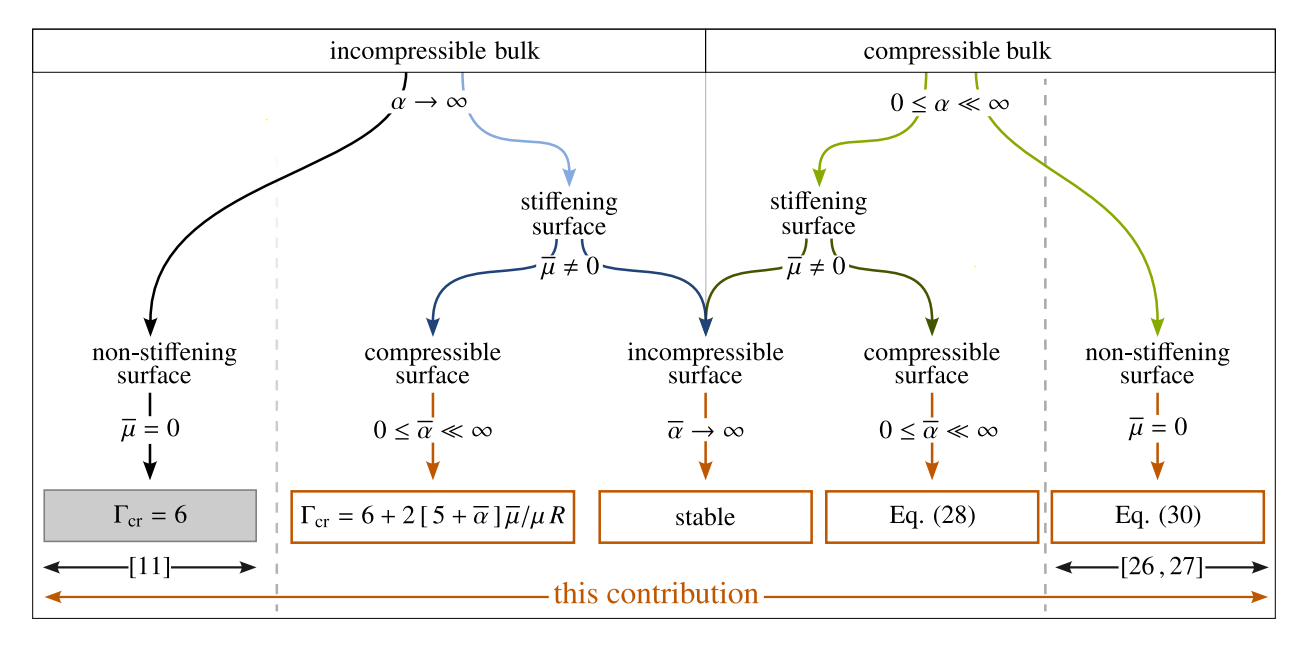


Figure 1: Overview of the gaps in literature that the current contribution aims to fill with the findings presented here, together with previous related works [9, 24, 25]. Surface incompressibility and increasing surface elasticity are found to render the structure stable. The parameters in the figure are defined as follows: \bar{v} : surface compressibility where $\bar{\alpha} := \bar{v}/(1-\bar{v})$. $\bar{\mu}$: surface elasticity. For the bulk, μ : shear modulus and v: Poisson's ratio where $\alpha := v/(1-v)$. R: initial fiber radius.

The remainder of the manuscript is organized as follows. Section 2 outlines the theoretical framework developed herein to capture the PR instability of compressible solids undergoing large deformations, accounting for the effects of *surface tension*, *surface elasticity* and *surface compressibility*. Section 3 contains a thorough deliberation on the results of the developed theoretical framework over a wide range of material parameters, analyzing the stability of the structure under various surface effects, presented together with numerical results. Finally, Section 4 concludes the work and provides further outlook.

2. Theory

Figure 2 depicts a continuum body that initially takes the material configuration $\mathcal{B}_0 \in \mathbb{R}^3$ at time t=0 with X denoting the reference placement of points of the bulk. The bulk of the material configuration is mapped to its spatial configuration $\mathcal{B}_t \in \mathbb{R}^3$ at a time t via the nonlinear deformation map φ according to $\mathbf{x} = \varphi(X,t)$ with \mathbf{x} denoting the placement of points in the deformed configuration. The bulk is endowed with an energetic surface, whose points are mapped from their material configuration $\partial \mathcal{B}_0$ to their spatial configuration $\partial \mathcal{B}_t$ through the mapping $\overline{\mathbf{x}} = \overline{\varphi}(\overline{X},t) = \varphi(X \in \partial \mathcal{B}_0,t)$. Note that in this contribution surface quantities are denoted as $\{\bullet\}$, and are distinguished from their bulk counterparts denoted as $\{\bullet\}$. The projection of the identity tensor I onto the surface is denoted as $\overline{I} = I - \overline{N} \otimes \overline{N}$, where \overline{N} is the unit normal to the surface in the material configuration, whereas \overline{n} denotes its spatial counterpart. The material line element dX is mapped to its spatial counterpart dx via the linear deformation map $dx = F \cdot dX$. Here, $F := \operatorname{Grad}\varphi$ is the deformation gradient for points in the bulk, and its determinant $J := \operatorname{Det} F$. The rank-deficient surface deformation gradient $\overline{F} = F \cdot \overline{I}$. Note that $[A \cdot B]_{ij} = A_{is} B_{sj}$ while the contraction of two second-order tensors A and B is denoted $A : B = A_{ij} B_{ij}$.

Remark on surface elasticity theory. How to formulate the thermodynamics of an energetic surface has been a riveting course of study for the past decades, following the seminal works of Scriven [34] looking into dynamic fluid interfaces and Gurtin and Murdoch [35] establishing a surface elasticity theory. Surface elasticity theory has since been widely applied to a variety of problems at the nanoscale, such as nanocomposites [36] and nanowires [37]. Surface energy and its thermodynamics has been further explored via the measurement of the surface energy at the nanoscale [38], or atomistic simulations [39]. Several works have proposed hyperelastic surface behavior [40–42], with some very recent methods being developed to measure and quantify the elastic properties of these surfaces [43, 44]. See [45, 46] for comprehensive reviews on surface elasticity.

Let P denote the first Piola stress. Quasi-static finite-deformation continuum mechanics, in the absence of body forces, is governed by the two fundamental equilibrium equations,

Div
$$P = 0$$
 and $P \cdot F^{t} = F \cdot P^{t}$ where $P := \frac{\partial \psi}{\partial F}$, (1)

the former dictating the balance of linear momentum and the latter the balance of angular momentum. The angular momentum balance here is satisfied a priori via the material frame indifference of the free energy density ψ per unit volume in the material configuration. The linear momentum balance, on the other hand, needs to be satisfied explicitly.

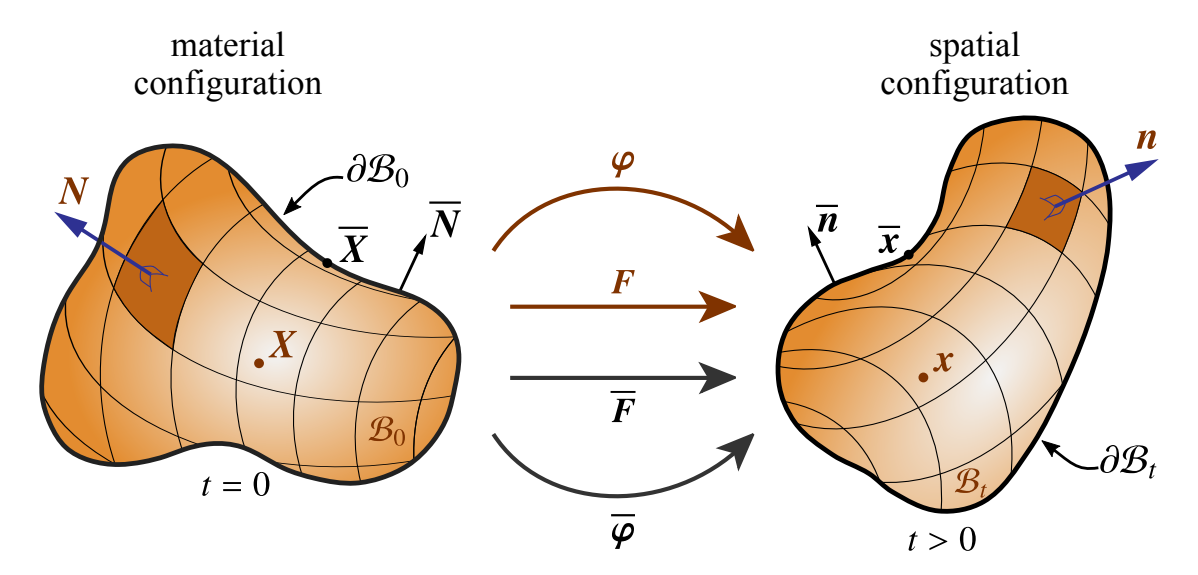


Figure 2: The continuum body at its material configuration $\mathcal{B}_0 \subset \mathbb{R}^3$ at time t = 0 is mapped its spatial configuration $\mathcal{B}_t \subset \mathbb{R}^3$ at any time t > 0 via the nonlinear deformation map φ , meanwhile the zero-thickness surface layer of the continuum body denoted as $\partial \mathcal{B}_0$ at its material configuration is mapped via the nonlinear deformation map $\overline{\varphi}$ to its spatial counterpart $\partial \mathcal{B}_t$.

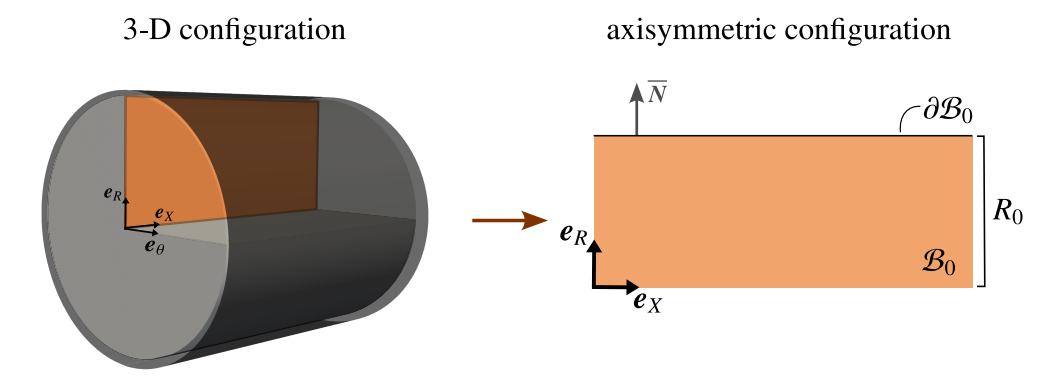


Figure 3: The cylindrical, 3D domain under question (left) and the corresponding axisymmetric configuration (right) that will be used in this work, along with the basis vectors e_x and e_r , and the unit outward surface normal \overline{N} . Note that axisymmetry is employed only for the analytical derivation while the computational framework remains fully three-dimensional.

In the absence of surface force densities the balance equations on the surface [47] read

$$\overline{\text{Div}}\,\overline{P} + P \cdot \overline{N} = 0 \quad \text{where} \quad \overline{P} := \frac{\partial \overline{\psi}}{\partial \overline{F}}, \tag{2}$$

where $\overline{\psi}$ denotes the free energy density per unit area of the surface in the material configuration and the surface divergence operator $\overline{\mathrm{Div}}\{\bullet\} := \mathrm{Grad}\{\bullet\} : \overline{I}$.

Constitutive models for material behavior are commonly based on a phenomenological free energy density [48]. Herein, the material behavior is assumed to be isotropic and homogeneous, hence the hyperelastic free energy density ψ is only a function of F. The behavior of the hyperelastic domain here will be modeled via a generic, compressible

neo-Hookean model [48] with the polyconvex free energy density of the form

$$\psi(\mathbf{F}) = \frac{1}{2}\mu \left[\mathbf{F} : \mathbf{F} - 3 - 2\ln J \right] + 2\mu \alpha f(J), \tag{3}$$

wherein μ is referred to as the *second Lamé parameter*, and the *first Lamé parameter* here is written out as the coefficient $2\mu\alpha$, using defined the parameter $\alpha:=\frac{\nu}{1-2\nu}$ for compressibility that ranges from full compressibility at $\alpha=0$ to incompressibility as $\alpha\to\infty$. Notice that the second part of the energy which is related to the compressibility of the domain can be any function of Jacobian $J:=\mathrm{Det} F$ as long as the energy density remains poly-convex. Typical examples of the function f(J) include

quadratic:
$$f(J) = \frac{1}{4} [J^2 - 1] - \frac{1}{2} \ln J$$
, logarithmic: $f(J) = \frac{1}{2} \ln^2 J$, (4)

among others. The Piola stress in the bulk obtained from the free energy density (3) reads

$$\mathbf{P} = \mu \left[\mathbf{F} - \mathbf{F}^{-t} \right] + 2\mu \alpha f' J \mathbf{F}^{-t} \quad \text{where} \quad f' := \frac{\partial f(J)}{\partial J} \quad \text{and} \quad \frac{\partial J}{\partial \mathbf{F}} = J \mathbf{F}^{-t}. \tag{5}$$

Analogously, the surface energy $\overline{\psi}$ reads

$$\overline{\psi}(\overline{F}) = \gamma \overline{J} + \frac{1}{2} \overline{\mu} \left[\overline{F} : \overline{F} - 2 - 2 \ln \overline{J} \right] + 2 \overline{\mu} \overline{\alpha} \overline{f}(\overline{J}) \quad \text{with} \quad \overline{f}(\overline{J}) := \frac{1}{4} \left[\overline{J}^2 - 1 \right] - \frac{1}{2} \ln \overline{J}, \tag{6}$$

where γ is the surface tension, $\overline{\mu}$ is surface elasticity, and $\overline{\alpha}$ is the surface compressibility parameter defined such that $\overline{\alpha} := \frac{\overline{\nu}}{1-\overline{\nu}}$ where $\overline{\nu}$ is the surface, two-dimensional Poisson's ratio ranging between $\overline{\nu} = 0$ at full compressibility and $\overline{\nu} \to 1$ at the limit of incompressibility. The surface Jacobian is defined as $\overline{J} := \overline{\operatorname{Det}} \overline{F}$, where the non-standard surface determinant operation reads $\overline{\operatorname{Det}} \overline{F} := \frac{1}{2} \left[\overline{F} : \overline{I} - \overline{F} : \overline{F} \right]$. In its most general form, the surface energy would include other surface invariants e.g. those that relate to capturing changing curvature, see for instance [49].

The corresponding surface Piola stress $\overline{P} := \partial \overline{\psi} / \partial \overline{F}$ reads

$$\overline{\boldsymbol{P}} = \gamma \, \overline{\boldsymbol{J}} \, \overline{\boldsymbol{F}}^{-t} + \overline{\mu} \left[\, \overline{\boldsymbol{F}} - \overline{\boldsymbol{F}}^{-t} \, \right] + \overline{\mu} \, \overline{\alpha} \left[\, \overline{\boldsymbol{J}}^2 - 1 \, \right] \, \overline{\boldsymbol{F}}^{-t} \,. \tag{7}$$

The problem that is dealt with here is axisymmetric, hence an axisymmetric formulation will be followed in this framework, as outlined in Fig. 3, wherein the orthonormal basis vectors e_x , e_r and e_θ have been shown. It is crucial to note that for this problem the basis vectors at the material and spatial configurations remain identical, i.e. $e_X \equiv e_x$ and $e_R \equiv e_r$, hence the notation e_x and e_r with the lower-case indices will be used to denote the basis vectors in the x and

r direction, respectively.

Starting with the problem formulation, uniform uniaxial tension/compression is applied to the axisymmetric domain in Fig. 3 such that the deformation gradient F reads

$$F = \lambda e_x \otimes e_x + \eta e_r \otimes e_r + \frac{r}{R} e_\theta \otimes e_\theta,$$
 (8)

where λ is the stretch in the axial direction, η denotes the transversal stretch, and r/R is the ratio of the deformed radius of the cylinder to its undeformed counterpart. Similarly, the surface counterpart of the deformation gradient, \overline{F} would be

$$\overline{F} = \lambda \, \boldsymbol{e}_{\scriptscriptstyle X} \otimes \boldsymbol{e}_{\scriptscriptstyle X} + \frac{r}{R} \, \boldsymbol{e}_{\scriptscriptstyle \theta} \otimes \boldsymbol{e}_{\scriptscriptstyle \theta} \,. \tag{9}$$

Explicitly satisfying the linear momentum balance of the bulk by using the deformation gradient (8) and established Piola stress (5), and assuming that all the stretches are constant along the domains, we obtain the key axisymmetry *relation*

$$Div \mathbf{P} = \mathbf{0} \quad \Rightarrow \quad \eta = r/R \,. \tag{10}$$

The relation (10) holds all throughout since here we look at solely the onset of the bifurcation, until which point the domain remains axisymmetric. Evaluating now the surface counterpart of the linear momentum balance given in Eq. (2), yields the *condition*

$$\overline{\text{Div}}\,\overline{P} + P \cdot \overline{N} = \mathbf{0} \quad \Rightarrow \quad \eta^2 + 2\,\alpha\,J\,f' + \Gamma\,\overline{J} + M\left[\eta^2 - 1 + \overline{\alpha}\left[\overline{J}^2 - 1\right]\right] - 1 = 0\,,\tag{11}$$

with

$$\Gamma := \frac{\gamma}{\mu R_0} \quad \text{and} \quad M := \frac{\overline{\mu}}{\mu R_0} \,,$$
 (12)

where Γ and M have been defined as unitless quantities that appear throughout the derivation, with R_0 denoting the initial cylinder radius. The quantity Γ has been identified in previous contributions as being the elastocapillary number. Herein by taking into account surface elasticity, we have uncovered another dimensionless parameter which we have denoted as M, which dictates the effect of surface elasticity. The condition stated in Eq. (11) allows for us to

calculate the resultant transverse stretch η from the applied lateral stretch λ , given the compressibility of the bulk α , the elastocapillary number Γ and surface elasticity number M and surface compressibility $\overline{\alpha}$, which renders it to be a non-linear Poisson's ratio equivalent. See [50] for more detailed deliberations on the non-linear Poisson's ratio.

Having satisfied the equilibrium equations of the deformed configuration, we will conduct an incremental stability analysis. To do so, we now perturb this configuration with an incremental displacement $\delta u := \delta u_x e_x + \delta u_r e_r$ and analyze the equilibrium of the perturbed state. In other words, the linear momentum balance now needs to be reevaluated such that we now look at the setting where $\text{Div}(P + \delta P) = 0$. Recall that DivP = 0 is already satisfied by imposing the relation (10); thus what remains is to evaluate the expression

$$Div\delta P = 0, \tag{13}$$

which will henceforth be referred to as the incremental linear momentum balance of the bulk. The incremental Piola stress δP is obtained via

$$\delta \mathbf{P} := \frac{\partial \mathbf{P}}{\partial \mathbf{F}} : \delta \mathbf{F} = \mu \, \delta \mathbf{F} + \left[1 - 2 \, \alpha \, J \, f' \, \right] \mathbf{D} + 2 \, \mu \, \alpha \, J \left[f' + J \, f'' \, \right] \mathbf{F}^{-t} : \delta \mathbf{F} \, \mathbf{F}^{-t} \,, \tag{14}$$

in which

$$\mathbf{D} := \frac{\partial \mathbf{F}^{-t}}{\partial \mathbf{F}} : \delta \mathbf{F} = -\mathbf{F}^{-t} \cdot \delta \mathbf{F}^{t} \cdot \mathbf{F}^{-t}, \tag{15}$$

where $\delta F := \operatorname{Grad} \delta u$ is the incremental deformation gradient. The solution to the instability where there is periodic wrinkling along the length of the domain is sought after here. Hence, the displacement functions δu_x and δu_r are assumed to be periodic in the x-direction with wavenumber k, such that we can readily write

$$\delta u_x = \delta u(r) \exp(ikx)$$
 and $\delta u_r = \delta v(r) \exp(ikx)$, (16)

where $\delta u(r)$ and $\delta v(r)$ are yet unknown functions of r and only r; thus for brevity henceforth the argument of these functions will be omitted and they will be simply referred to as δu and δv and their derivatives with respect to r will be denoted $\{\bullet\}' = d\{\bullet\}/dr$. Having defined the incremental displacement functions and incremental deformation gradient

 δF , the explicit form of Eq. (14) can be written as

$$\delta \mathbf{P} = \left[\left[1 + \omega \eta^{4} \right] i k \delta u + \lambda \eta^{3} \left[\omega - D \right] \left[\delta v' + \frac{\delta v}{R} \right] \right] \mathbf{e}_{x} \otimes \mathbf{e}_{x}
+ \left[\delta u' + D \lambda \eta^{3} i k \delta v \right] \mathbf{e}_{x} \otimes \mathbf{e}_{r} + \left[i k \delta v + D \lambda \eta^{3} \delta u' \right] \mathbf{e}_{r} \otimes \mathbf{e}_{x}
+ \left[\left[1 + \omega \lambda^{2} \eta^{2} \right] \delta v' + \lambda^{2} \eta^{2} \left[\omega - D \right] \frac{\delta v}{R} + \lambda \eta^{3} \left[\omega - D \right] i k \delta u \right] \mathbf{e}_{r} \otimes \mathbf{e}_{r}
+ \left[\left[1 + \omega \lambda^{2} \eta^{2} \right] \frac{\delta v}{R} + \lambda^{2} \eta^{2} \left[\omega - D \right] \delta v' + \lambda \eta^{3} \left[\omega - D \right] i k \delta u \right] \mathbf{e}_{\theta} \otimes \mathbf{e}_{\theta},$$
(17)

where

$$D := \frac{1}{J^2} - \frac{2\alpha}{J} \frac{\partial f}{\partial J} \quad \text{and} \quad \omega := \frac{1}{J^2} + 2\alpha \frac{\partial^2 f}{\partial J^2}.$$
 (18)

It should be noted that at the incompressibility limit where J=1, the constant $\omega=D+2\alpha$, regardless of f, and the relation for $D:=\eta^2+\Gamma\lambda\eta+M\left[\eta^2-1+\overline{\alpha}\left[\overline{J}^2-1\right]\right]$ can be obtained from (11). Using the incremental Piola stress (17) in the incremental linear momentum balance (13) yields a set of differential equations which read

$$\operatorname{Div}\delta\boldsymbol{P} = 0 \quad \Rightarrow \quad \begin{cases} \delta u'' + \frac{\delta u'}{R} - \left[1 + \omega \eta^4\right] k^2 \, \delta u + \omega i k \lambda \eta^3 \left[\delta v' + \frac{\delta v}{R}\right] = 0, \\ \left[1 + \omega \lambda^2 \eta^2\right] \left[\delta v'' + \frac{\delta v'}{R} - \frac{\delta v}{R^2}\right] - k^2 \, \delta v + \omega i k \lambda \eta^3 \, \delta u' = 0. \end{cases}$$

$$(19)$$

The system (19) is a system of partial differential equations, in terms of the incremental displacement functions δu and δv and their derivatives. The intermediary steps for solving this system of differential equations have been omitted here for the sake of brevity and can be found in Appendix A. Solving the system (19) following the steps outlined in Appendix A yields the final set of results

$$\begin{cases} \delta u = \frac{i}{N^{2} \omega k^{3} \lambda \eta^{3}} \left[\delta v''' + \frac{2\delta v''}{R} - \frac{\delta v'}{R^{2}} + \frac{\delta v}{R^{3}} \right] - \frac{\left[1 - \omega^{2} \lambda^{2} \eta^{6} \right] i}{\left[1 + \omega \eta^{4} \right] \omega k \lambda \eta^{3}} \left[\delta v' + \frac{\delta v}{R} \right], \\ \delta v = C_{1} I_{1}(kNR) + C_{2} k N \left[K_{1}(kNR) \int_{R}^{R_{0}} s I_{1}(ks) I_{1}(kNs) ds - I_{1}(kNR) \int_{R}^{R_{0}} s I_{1}(ks) K_{1}(kNs) ds \right], \end{cases}$$
(20)

with

$$N^2 := \frac{1 + \omega \,\eta^4}{1 + \omega \,\lambda^2 \,\eta^2} \,, \tag{21}$$

where C_1 and C_2 are unknown constants to be determined, and I_1 and K_1 are first-order modified Bessel functions of

the first and second kind, respectively. At the incompressibility limit, $N = \lambda \sqrt{\lambda}$ which results in N = 1 for the case of no stretch i.e. $\lambda = 1$.

Having obtained the necessary solutions for the incremental displacement functions, we now apply the boundary conditions of the problem to solve for the remaining unknowns C_1 and C_2 , and hence the onset of bifurcation. To this extent, we only have one boundary condition at the surface $R = R_0$ where R_0 is the initial cylinder radius, which reads

$$\overline{\mathrm{Div}}\delta\overline{\boldsymbol{P}}\bigg|_{R=R_0} = \delta\boldsymbol{P}\cdot\boldsymbol{N}\bigg|_{R=R_0},\tag{22}$$

wherein the incremental surface Piola stress, $\delta \overline{P}$, is defined as

$$\delta \overline{\boldsymbol{P}} = \gamma \overline{J} \left[\overline{\boldsymbol{F}}^{-t} : \delta \overline{\boldsymbol{F}} \, \overline{\boldsymbol{F}}^{-t} + \overline{\boldsymbol{D}} \right] + \overline{\mu} \left[\delta \overline{\boldsymbol{F}} - \overline{\boldsymbol{D}} \right] + \overline{\mu} \overline{\alpha} \left[\left[\overline{J}^2 - 1 \right] \left[\overline{\boldsymbol{D}} \right] + 2 \overline{J}^2 \, \overline{\boldsymbol{F}}^{-t} : \delta \overline{\boldsymbol{F}} \, \overline{\boldsymbol{F}}^{-t} \right], \tag{23}$$

where

$$\overline{\boldsymbol{D}} := \frac{\partial \overline{\boldsymbol{F}}^{-\mathsf{t}}}{\partial \overline{\boldsymbol{F}}} : \delta \overline{\boldsymbol{F}} = -\overline{\boldsymbol{F}}^{-\mathsf{t}} \cdot \delta \overline{\boldsymbol{F}}^{\mathsf{t}} \cdot \overline{\boldsymbol{F}}^{-\mathsf{t}} + \frac{1}{\lambda^2} \delta \overline{\boldsymbol{F}}^{\mathsf{t}} : [\boldsymbol{T} \otimes \boldsymbol{N}] \boldsymbol{N} \otimes \boldsymbol{T},$$
(24)

where T is the unit tangent vector to the outer surface, i.e. $T := e_x$, and $\delta \overline{F} = \delta F \cdot \overline{I}$. The incremental surface Piola stress thus explicitly reads

$$\delta \overline{P} = \left[\overline{\mu} ik \, \delta u \left[1 + \overline{\omega} \, \eta^2 \right] + \frac{\delta v}{R} \left[\gamma + 2 \overline{\mu} \, \overline{\alpha} \, \lambda \, \eta \right] \right] e_x \otimes e_x + \left[\overline{\mu} ik \, \delta v \left[1 + \overline{D} \, \eta^2 \right] + \delta v \, \frac{\gamma ik \, \eta}{\lambda} \right] e_r \otimes e_x \\
+ \left[\overline{\mu} \, \frac{\delta v}{R} \left[1 + \overline{\omega} \, \lambda^2 \right] + \delta u \, ik \left[\gamma + 2 \, \overline{\mu} \, \overline{\alpha} \, \lambda \, \eta \right] \right] e_\theta \otimes e_\theta. \tag{25}$$

where

$$\overline{D} := \frac{1 - \overline{\alpha} [\overline{J}^2 - 1]}{\overline{J}^2} \quad \text{and} \quad \overline{\omega} := \overline{D} + 2 \overline{\alpha}.$$
 (26)

We can now evaluate the boundary condition at the surface (22), which yields the system of equations

$$\begin{bmatrix}
ik \frac{\delta v}{R_0} \left[\gamma + 2 \overline{\mu} \overline{\alpha} \lambda \eta \right] - \overline{\mu} k^2 \delta u \left[1 + \overline{\omega} \eta^2 \right] \\
-\delta v \left[\overline{\mu} k^2 \left[1 + \overline{D} \eta^2 \right] + \frac{\gamma \eta}{\lambda} k^2 + \frac{\overline{\mu}}{R_0^2} \left[1 + \overline{\omega} \lambda^2 \right] \right] - \frac{ik \delta u}{R_0} \left[\gamma + 2 \overline{\mu} \overline{\alpha} \lambda \eta \right] \end{bmatrix}$$

$$= \begin{bmatrix}
\mu \delta u'(R_0) + \mu Dik \lambda \eta^3 \delta v(R_0) \\
\mu \left[1 + \omega \lambda^2 \eta^2 \right] \delta v'(R_0) + \mu \lambda^2 \eta^2 \left[\omega - D \right] \frac{\delta v(R_0)}{R_0} + \mu ik \lambda \eta^3 \left[\omega - D \right] \delta u(R_0) \end{bmatrix}.$$
(27)

The first row of (27) allows for us to solve for the constant C_2 , which can then be used in evaluating the second row in (27) to obtain the final solution. By looking at this solution of the system over a wide range of wavelength k, we can see that the long-wave form with k = 0 is always, for all material parameters and stretches, the preferred mode of instability. Hence, we will evaluate our solution at the limit if $k \to 0$ and simplify, rendering the condition

$$2\left[\Gamma + \left[\omega - D\right]\lambda\eta^{3} + 2M\overline{\alpha}\lambda\eta\right]^{2} - \left[2M\left[1 + \overline{\omega}\eta^{2}\right] + 1 + \omega\eta^{4}\right]\left[1 + \omega\lambda^{2}\eta^{2} + \left[\omega - D\right]\lambda^{2}\eta^{2} + M\left[1 + \overline{\omega}\lambda^{2}\right]\right] \stackrel{!}{=} 0,$$
(28)

which is the final solution for the long-wave instability of an axisymmetric compressible domain as functions of surface tension, surface elasticity, surface compressibility and bulk shear modulus and compressibility. The Eq. (28) can be solved for critical stretch λ_{cr} or critical elastocapillary number Γ_{cr} to obtain the onset of bifurcation, using the relation uncovered in Eq. (11) to calculate vertical stretch η from the applied stretch λ and elastocapillary number Γ , surface elasticity parameter M and surface compressibility $\overline{\alpha}$. Note that in the absence of surface effects where M=0 Eq. (28) renders a solution for the instability of a compressible domain under surface tension, which reads

$$2\left[\Gamma + [\omega - D]\lambda \eta^{3}\right]^{2} - \left[1 + \omega \eta^{4}\right]\left[1 + \omega \lambda^{2} \eta^{2} + [\omega - D]\lambda^{2} \eta^{2}\right] \stackrel{!}{=} 0.$$
 (29)

Due to accounting for the compressibility of the bulk and hence the complex dependence of η on λ , α , Γ , M and $\overline{\alpha}$, it is not possible to obtain an open form solution of Eq. (28) at its most generic form. However, for an incompressible bulk where $\nu \to 0.5$ or $\alpha \to \infty$, an explicit solution can be obtained from Eq. (11) such that $\eta = 1/\sqrt{\lambda}$. This allows us to simplify the bifurcation equation (28) at $\alpha \to \infty$ to render an explicit solution for critical elastocapillary number such that

$$\Gamma_{\rm cr} = \frac{2[2+\lambda^3]}{\lambda\sqrt{\lambda}} + \frac{2M}{\lambda\sqrt{\lambda}} \left[2\lambda^3 + [1+\overline{\alpha}]\lambda + 2 \right]. \tag{30}$$

Equation (30) presents, for the first time, an explicit solution for the critical elastocapillary number, or surface tension, of an incompressible fiber undergoing stretch λ while taking into account surface elasticity and area compressibility. Note that the solution remains independent of the energy function used, since they exhibit identical behavior at the incompressible limit. The solution in Eq. (30) illustrates clearly that the two surface parameters M and $\overline{\alpha}$ do not act independently, but that there exists an effective parameter as a combination of the two, together with the applied stretch. This effective parameter can be more clearly seen for the case of applied stretch $\lambda = 1$, where the solution

further reduces to

$$\Gamma_{\rm cr} = 6 + 2\left[5 + \overline{\alpha}\right]M. \tag{31}$$

For the case of no surface effects, i.e. M = 0, the solution (30) reduces to the well-known incompressible solution [20]

$$\Gamma_{\rm cr} = \frac{2\left[2 + \lambda^3\right]}{\lambda \sqrt{\lambda}},\tag{32}$$

which if further reduced to the case where there is no applied stretch i.e. $\lambda = 1$ clearly captures the classical solution of $\Gamma_{cr} = 6$ [9].

3. Results and Discussion

This section explores the results of the developed theoretical framework for a variety of material parameters, presenting the theoretical results together with numerical results from surface-enhanced isogeometric analysis with eigenvalue analysis. Axisymmetry assumptions have been made to simplify the calculations in the theoretical derivations. However, the numerical framework is fully three-dimensional and not limited to axisymmetric deformations. Comparing the numerical and theoretical results confirms that assuming axisymmetry in the theoretical derivations does not lead to any information loss. For the post-bifurcation behavior of the structure and the effect of bulk compressibility and surface tension, the readers are directed to recent work [24], ignoring the surface compressibility and stiffening. However, the post-instability analysis counterpart of this work considering surface effects including surface tension, surface stiffening, and area compressibility remains outside the scope of the current contribution as it requires an in-depth analysis on its own.

In this section, the critical values of elastocapillary number Γ_{cr} and overall stretch λ_{cr} at which the structure becomes unstable are solved for using the bifurcation equation (28), given the material parameters. The quadratic (4)₁ and logarithmic (4)₂ energy functions f(J) will be used in the following examples. However, it should be noted that the framework remains generic and virtually applicable to any arbitrary but meaningful function f(J). Accordingly, first the bifurcation behavior of an incompressible, stretched domain with surface stiffening and surface compressibility is examined. Next, the analysis is carried out for a compressible bulk, and varying applied stretches, presenting results together with numerical findings. Finally, the individual effects of surface stiffening and area compressibility on instability behavior are elaborated on.

Figure 4 illustrates the findings and limits of the key bifurcation relation Eq. (30). Bifurcation curves for an in-

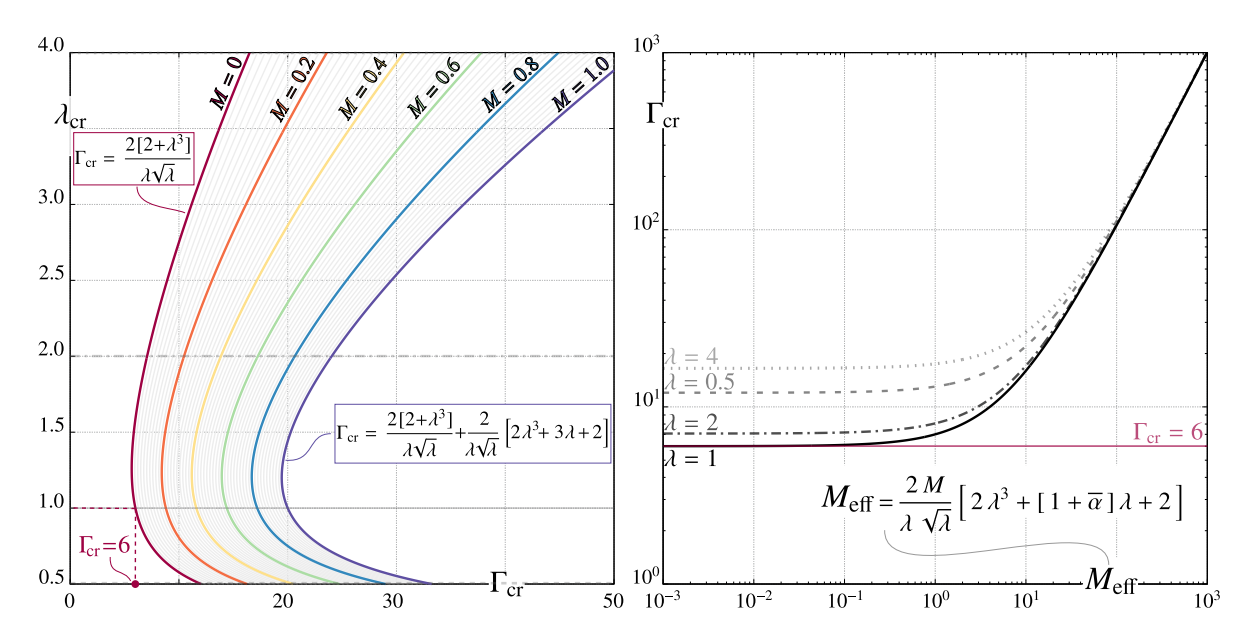


Figure 4: Analytical results associated with an incompressible bulk and fully compressible surface $\bar{\alpha}=0$ obtained via Eq. (30) for $\Gamma_{\rm Cr}$ vs. $\lambda_{\rm Cr}$, for various values of dimensionless surface elasticity number $M:=\bar{\mu}/\mu R_0$ (left). $\Gamma_{\rm Cr}$ plotted against effective surface parameter $M_{\rm eff}$ for certain values of stretch λ is shown on the right.

compressible bulk undergoing stretch λ and prescribed elastocapillary number Γ_{cr} are depicted for a range of surface elasticity numbers $M := \overline{\mu}/\mu R_0$ on the left. Clearly, the limits previously established in literature are recovered, in addition to providing explicit solutions to the bifurcation curves of structures with various surface elasticity parameters. As M increases, the curves shift towards higher critical surface tension values, showing that increased surface elasticity precludes the instability behavior. Looking at the expression (31), it can be seen that the second term is composed of both surface elasticity number M and area compressibility parameter $\overline{\alpha}$, together with applied stretch λ . This means that the two surface parameters act in conjunction to render an effective stiffening parameter M_{eff} for the surface, which for the incompressible case can be defined explicitly as

$$M_{\text{eff}} := \frac{2M}{\lambda \sqrt{\lambda}} \left[2\lambda^3 + \left[1 + \overline{\alpha} \right] \lambda + 2 \right]. \tag{33}$$

This is expected since the problem at hand is axisymmetric, hence the change of volume and area of the surface are intrinsically related. The graph on the right of Fig. 4 plots critical elastocapillary numbers for a set of prescribed stretches λ , over changing effective surface parameter $M_{\rm eff}$. As $M_{\rm eff} \to 0$ we see that the solution approaches the classical case with no surface effects. The horizontal asymptotes further illustrate how changing the applied stretch λ can render the structure undergoing the same surface tension stable/unstable. On the other hand, as $M_{\rm eff} \to \infty$, the surface tension needed to initiate the instability (i) increases without bounds, and (ii) becomes identical for all applied stretches. All together, the results illustrate that at the onset of the instability, the behavior of an incompressible

bulk is governed by the applied stretch, and a combination of the elasticity and area compressibility of the surface, specifically via the relation (33).

Next, the behavior of a slightly more compressible bulk at v = 0.4 is examined in Fig. 5, comparing the results to numerical findings also. An excellent agreement between the analytical and numerical solutions is established for the infinite-wavelength solutions. The left inset of Fig. 5 displays the bifurcation curves over changing surface elasticity parameter M, while the right inset shows the same curves for changing surface compressibility $\bar{\nu}$. Clearly, increasing surface elasticity M and increasing the surface compressibility parameter $\bar{\nu}$ have the same effect: precluding the instability behavior. Furthermore, compared with the curves in Fig. 4 for the incompressible bulk, the curves here for the more compressible bulk display zero-slope regions towards increasing surface tension. These zero-slope regions mean analytically that the onset of instability of the structure loses its dependence on the applied stretch. Notice that these horizontal asymptotes move downward with increasing surface elasticity, meaning that more configurations become stable as M or $\bar{\nu}$ are increased. The physical interpretation of this is that with a compressible bulk, there exists a limit for stretch λ above which the structure remains stable regardless of stretch or surface tension, and that this limit can be shifted by changing surface parameters. This suggests that tuning the bulk compressibility, together with the surface elasticity and surface compressibility, may render the structure stable.

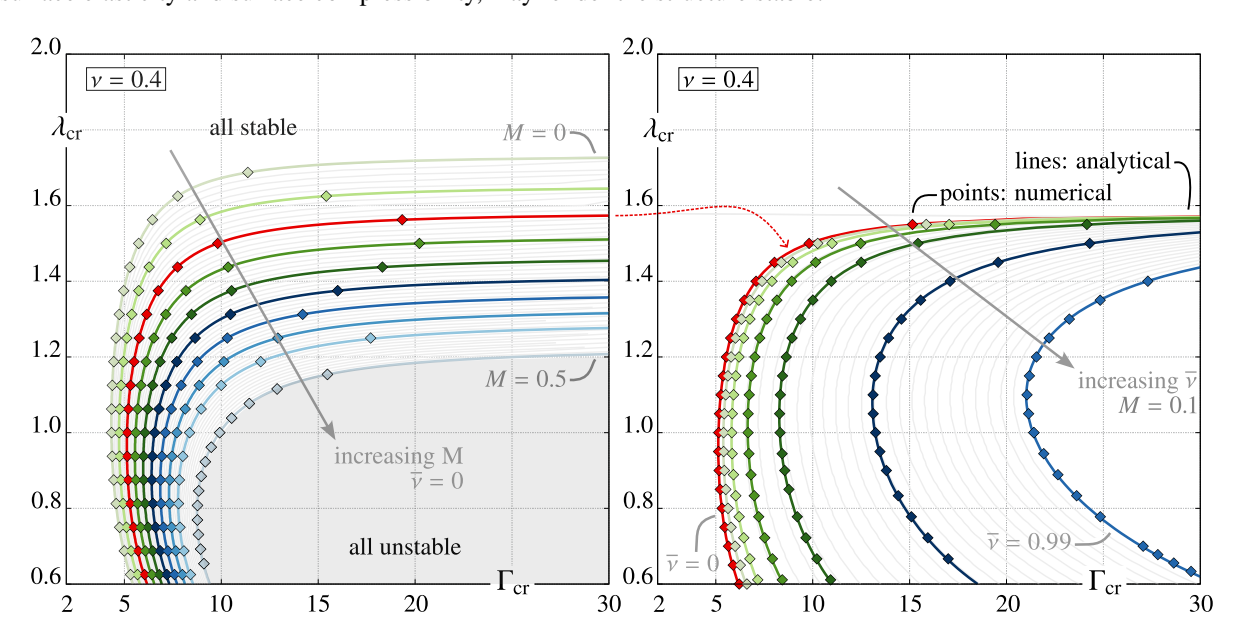


Figure 5: Analytical results obtained via Eq. (28) for $\lambda_{\rm CT}$ vs. $\Gamma_{\rm CT}$ for various values of dimensionless surface elasticity number $M:=\overline{\mu}/\mu R_0$ (left), and area compressibility $\overline{\nu}$ (right), displayed together with numerical results obtained via isogeometric FEM enhanced with eigenvalue analysis. Note that the gray shaded area denotes the region where all points are unstable, while the area that remains above the curves denotes the stable regions.

Figure 6 illustrates further the effect of different bulk compressibilities on the bifurcation curves plotted over criti-

cal stretch and critical elastocapillary number, for increasing surface elasticity and for two different energy functions. In general, the upper limit of stretches where an unstable configuration is possible significantly decreases with increasing compressibility. Also, the flattening out behavior seen for the quadratic energy is not apparent for the logarithmic energy. This means that the energy function used can be crucial in determining whether the structure would be stable given a set of material parameters. This further illustrates the utility of the framework since it allows for the use of any strain energy function of the form (3), which can be chosen to be the most suitable one for the materials to be used in the desired applications.

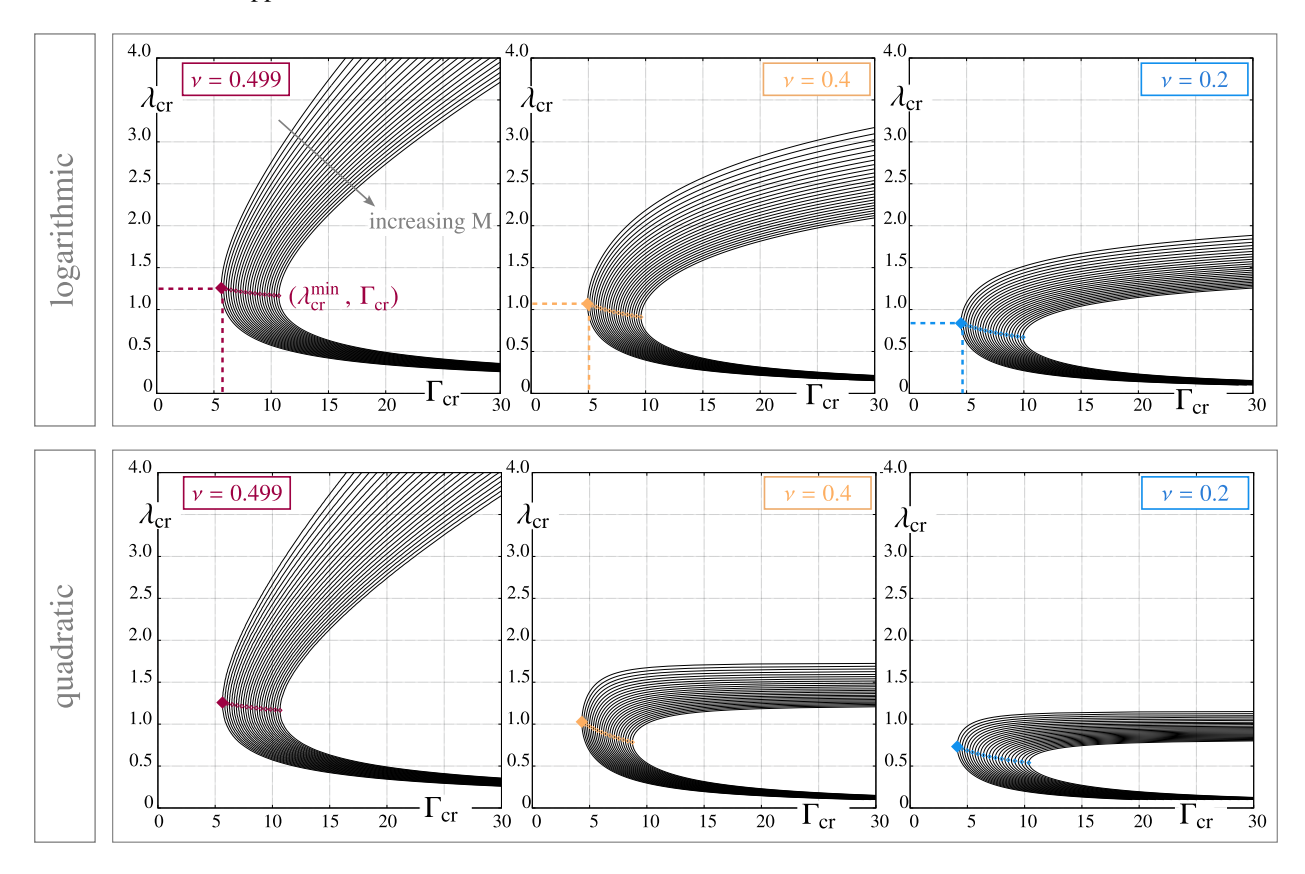


Figure 6: Critical stretch $\lambda_{\rm Cr}$ vs. critical elastocapillary number $\Gamma_{\rm Cr}$, for increasing surface elasticity number M, for various values of bulk compressibility $\nu=0.499$, $\nu=0.4$, and $\nu=0.2$. The minimums of these curves at $(\Gamma_{\rm cr}^{min}, \lambda_{\rm cr})$ are marked, denoting the minimitum threshold for the elastocapillary number and corresponding critical stretch for the onset of instability. Results are given for both logarithmic (top) and quadratic (bottom) energy functions.

Looking further into how bulk compressibility can be tuned to manipulate the instability behavior of the structures, Fig. 7 plots how critical elastocapillary number changes over changing bulk compressibility, under stretch $\lambda = 1$, for changing values of M (left), ranging from vanishing surface elasticity M = 0 to a slight surface stiffening M = 0.5 and surface compressibility \bar{v} (right) from a fully compressible surface $\bar{v} = 0$ towards a nearly incompressible one $\bar{v} = 0.95$, presented together with numerical results. For the whole range of material parameters an excellent agreement between

the analytical and numerical results is observed. Furthermore, once again, it is clear that also over changing bulk compressibility, increasing M and \bar{v} have a qualitatively similar effect on bifurcation behavior. For vanishing surface effects, as the bulk approaches the fully compressible limit at v = 0, the surface tension needed to initiate the instability sharply increases. This result implies that a fully compressible bulk is stable, regardless of the surface tension it undergoes. Since for a fully compressible bulk there is virtually no stretch in the vertical direction under any horizontal stretch, and due to the axisymmetry of the problem, there is not enough stress developed in the material to trigger the instability. As surface elasticity or surface incompressibility is increased, more surface tension is needed to initiate the instability for each bulk compressibility v. What is interesting about the data in this figure is that the asymptote at v = 0 for vanishing surface elasticity, M = 0, shifts to the right (towards higher compressibility values) as M increases, while the same behavior holds for increasing \bar{v} with a constant M. Hence, with increasing surface elasticity or surface compressibility, a larger portion of the bulk compressibility domain becomes stable. These two important observations together render the conclusion that surface elasticity and surface incompressibility precludes the PR instability for compressible domains.

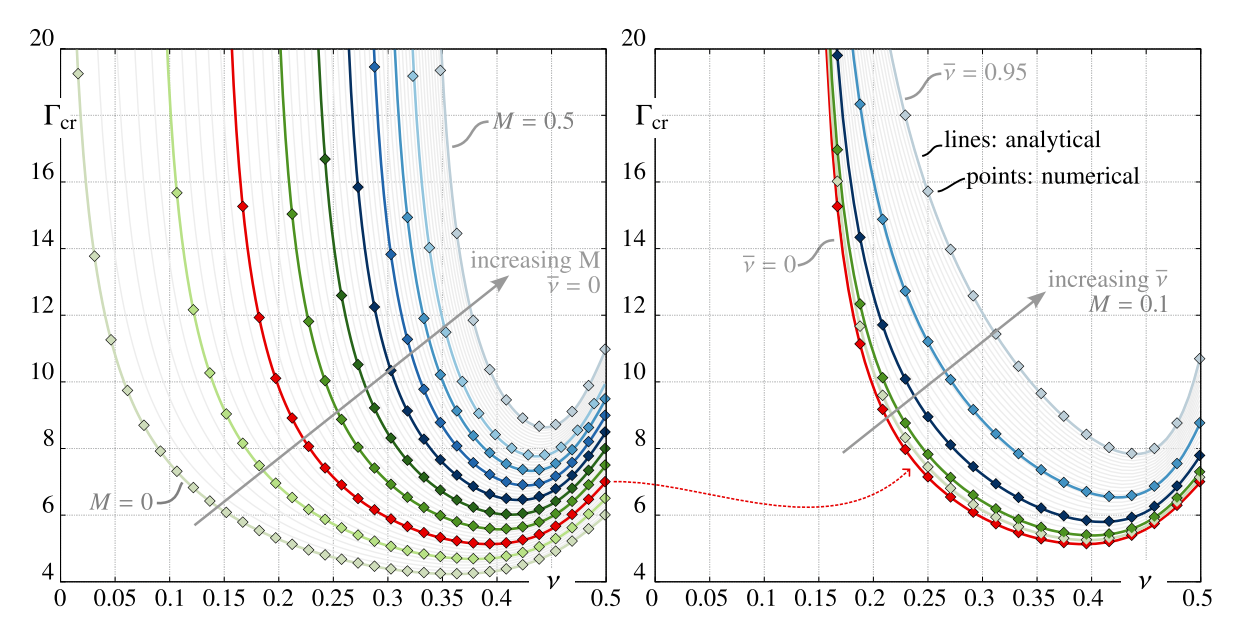


Figure 7: Analytical results obtained via Eq. (28) for $\Gamma_{\rm Cr}$ vs. ν , for various values of dimensionless surface elasticity number $M:=\overline{\mu}/\mu R_0$ (left), and area compressibility $\overline{\nu}$ (right), displayed together with numerical results obtained via isogeometric FEM enhanced with eigenvalue analysis.

To evaluate the effect of surface compressibility on the onset of instability of compressible domains in more detail, we look at Fig. 8, where now the critical elastocapillary number Γ_{cr} is plotted against changing surface compressibility $\overline{\nu}$. Changing bulk compressibility ν is depicted in the various insets, and increasing surface elasticity M is denoted by the colorbar and the corresponding contour lines. As $\overline{\nu} \to 0$ the curve flattens out for all material parameters. On the

other hand, there exists an asymptote at $\overline{\nu} \to 1$ for all bulk Poisson's ratios and $\overline{\mu}$ values. These together suggest that surface incompressibility has a significant effect on bifurcation behavior, with a fully incompressible surface rendering the structure stable regardless of bulk compressibility or surface elasticity. Surface incompressibility is a phenomenon that has been observed in biological cell membranes, such as in red blood cells, and plays a critical role in their mechanics. Surface of metal structures, e.g. nanobeams, posses significant stiffening/softening effects and assumed to have the same compressibility as the bulk [39]. The combination of a compressible bulk with an incompressible surface, or vice versa, for example see recently published [51], or the range of acceptable combinations of surface and bulk parameters remains elusive and we hope that the developed framework will shed light on our understanding of this issue.

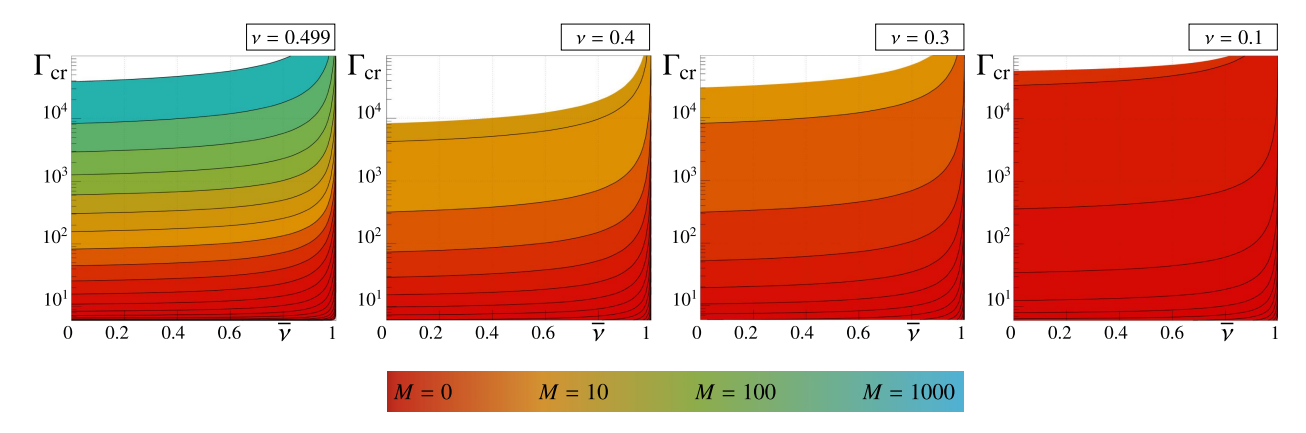


Figure 8: $\Gamma_{\rm Cr}$ vs. $\overline{\nu}$, for $\overline{\mu}=0.1$ and varying bulk Poisson's ratio from $\nu=0.499$ (left-most) to $\nu=0.1$ (right-most), for changing $M:=\overline{\mu}/\mu R_0$ denoted by the colorbar and contour lines.

Finally, to observe the effect of surface elasticity parameter M in more detail, Fig. 9 further looks into a wide range of surface elasticity M with $\bar{\nu}=0$. Marking the asymptote of the critical elastocapillary number, as shown in the three dimensional surface graphs (Fig. 9), renders a limit curve in the parameter space of bulk compressibility ν and surface elasticity M, shown in the 2D center insets. The region below the limit curve marks the points where the structure is stable regardless of the surface tension applied. The region above the curve denotes points at which there exists a non-infinite value of surface tension that can render the structure unstable. For surface elasticity M=0, an unstable configuration exists for all values of compressibility except for the limit of vanishing Poisson's ratio $\nu \to 0$ of the bulk. As $M \to \infty$ the domain becomes stable since the limit is reached where only stable configurations exist for any value of Poisson's ratio. In summary, increasing surface elasticity has a stabilizing effect for all bulk compressibility values. Current methods for increasing surface elasticity include applying thin film coatings [52], applying UV radiation to elastomer surfaces [2] or through shrinking or mold effects in hydrogels [5]. Recent works have begun to investigate

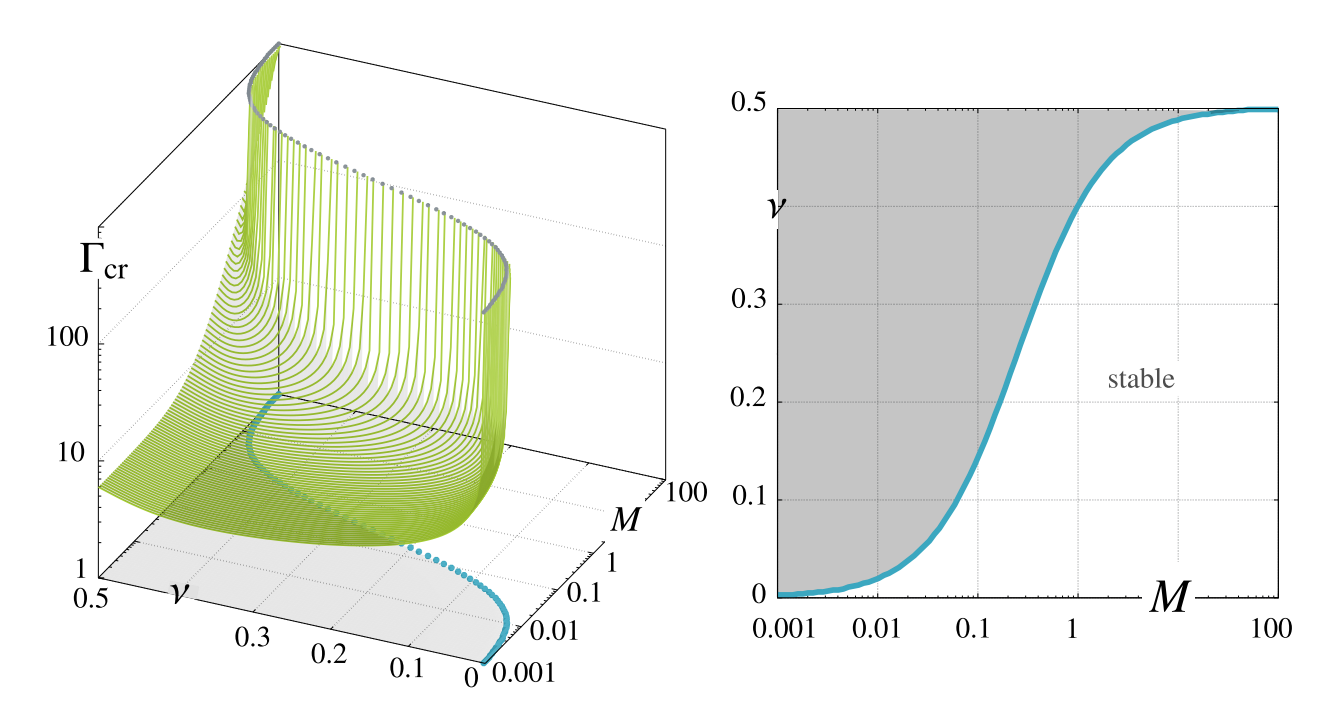


Figure 9: Surface for $\Gamma_{\rm Cr}$ vs. ν vs. $M:=\overline{\mu}/\mu R_0$ for quadratic bulk energy and corresponding stability curve, wherein the white region denotes the stable points and the gray region denotes points where there exists an unstable configuration for the given material parameters. Once again $\overline{\alpha}=0$ and $\lambda=1$.

the measurement and characterization techniques of soft, surface properties [43, 44].

4. Conclusion

We have derived an analytical solution to solve for the onset of the PR instability in soft solids with surface tension, surface elasticity and area compressibility, following an incremental stability analysis under a large-deformations, compressible framework. An explicit analytical solution to predict the critical surface tension for the onset of instability of an incompressible bulk with surface stiffening and area compressibility effects has been presented, for the first time. A novel dimensionless parameter *M* relating to surface elasticity was found to significantly effect the bifurcation behavior of the structure in conjunction with surface compressibility. This is crucial because until now, only surface tension and applied stretch have been regarded as the governing mechanisms for the fiber beading instability. In this work, we (i) establish that surface stiffening and area compressibility play a crucial role in the onset of the instability, and (ii) outline the underlying mechanism and explicit solutions regarding exactly *how* these surface parameters affect the instability behavior. More specifically, it is seen that surface elasticity and surface incompressibility preclude the PR instability in soft, compressible solids. This is especially vital for applications wherein the fiber beading instability is an unwanted by-product or needs to be tuned; the findings clearly demonstrate how the instability behavior can be avoided or triggered simply by manipulating the surface properties of the materials. Our next immediate course is to

take into account the boundary viscoelasticity [53, 54] and flexural stiffness [52, 55] of the surface in the developed framework. The acceptable range and combination of surface parameters and bulk parameters, as well as other, non-infinite wavelength modes and post-bifurcation behavior of the structure under surface effects remain open questions to be answered in following works.

Acknowledgment

ADB and BD acknowledges funding from the National Science Foundation (NSF) through the DMREF program under grant number CMMI 2119716.

Appendix A. Detailed solution to Eq. (19)

The system in (19) can be written out using specific operators to be able to perform linear operations on the expressions with higher order derivatives, such that

$$\begin{cases} \mathcal{L}_{2}(\delta u) + \omega ik \lambda \eta^{3} \mathcal{L}_{3}(\delta v) &= 0\\ \frac{\omega ik \lambda \eta^{3}}{1 + \omega \lambda^{2} \eta^{2}} \mathcal{L}_{4}(\delta u) + \mathcal{L}_{5}(\delta v) &= 0. \end{cases}$$
(A.1)

where the operators \mathcal{L}_i have been defined as

$$\mathcal{L}_{2}\{\bullet\} := \frac{\mathrm{d}^{2}\{\bullet\}}{\mathrm{d}R^{2}} + \frac{1}{R} \frac{\mathrm{d}\{\bullet\}}{\mathrm{d}R} - \left[1 + \omega \eta^{4}\right] k^{2}\{\bullet\},
\mathcal{L}_{3}\{\bullet\} := \frac{\mathrm{d}\{\bullet\}}{\mathrm{d}R} + \frac{\{\bullet\}}{R},
\mathcal{L}_{4}\{\bullet\} := \frac{\mathrm{d}\{\bullet\}}{\mathrm{d}R},
\mathcal{L}_{5}\{\bullet\} := \frac{\mathrm{d}^{2}\{\bullet\}}{\mathrm{d}R^{2}} + \frac{1}{R} \frac{\mathrm{d}\{\bullet\}}{\mathrm{d}R} - \frac{\{\bullet\}}{R^{2}} - \frac{k^{2}\{\bullet\}}{1 + \omega \lambda^{2} \eta^{2}}.$$
(A.2)

Simultaneously solving the two equations renders the one-dimensional differential equation

$$\omega ik \lambda \eta^3 \mathcal{L}_3(\delta v) - \frac{1 + \omega \lambda^2 \eta^2}{\omega ik \lambda \eta^3} \mathcal{L}_2(\mathcal{L}_4^{-1}(\mathcal{L}_5(\delta v))) = 0, \tag{A.3}$$

which clearly is only a function of δv and can be rewritten in its simpler form

$$\mathcal{L}_0\left(\mathcal{L}_1(\delta v)\right) = 0\,,\tag{A.4}$$

wherein the new operators are defined as

$$\mathcal{L}_{0}\{\bullet\} := \frac{\mathrm{d}^{2}\{\bullet\}}{\mathrm{d}R^{2}} + \frac{1}{R} \frac{\mathrm{d}\{\bullet\}}{\mathrm{d}R} - \frac{\{\bullet\}}{R^{2}} - k^{2}\{\bullet\},$$

$$\mathcal{L}_{1}\{\bullet\} := \frac{\mathrm{d}^{2}\{\bullet\}}{\mathrm{d}R^{2}} + \frac{1}{R} \frac{\mathrm{d}\{\bullet\}}{\mathrm{d}R} - \frac{\{\bullet\}}{R^{2}} - k^{2}N^{2}\{\bullet\}.$$
(A.5)

Now, for the sake of brevity let us define the following $a(R) := \mathcal{L}_1(\delta v)$, which simplifies Eq. (A.4) to the simple differential equation in terms of a, reading

$$\mathcal{L}_0(a) = \frac{d^2 a}{dR^2} + \frac{1}{R} \frac{da}{dR} - \frac{a}{R^2} - k^2 a = 0, \tag{A.6}$$

which can be rewritten as

$$R^2 a'' + R a' - [k^2 R^2 + 1] a = 0, (A.7)$$

which is clearly a homogenous modified Bessel equation with order n = 1, with the solution

$$a = C_2 I_1(kR) + C K_1(kR). (A.8)$$

wherein I_1 and K_1 are modified Bessel functions of the first and second kind, respectively, of order one, and C_2 and C are arbitrary constants. Since our domain is a cylinder and we expect to have a finite value as $R \to 0$, and since the function $K_1(kR)$ diverges at $R \to 0$, we establish that the constant C = 0. Moving forward, and using the definition of C and the uncovered solution (A.8), we can solve for

$$\mathcal{L}_1(\delta v) = a \quad \Rightarrow \quad \delta v^{\prime\prime} + \frac{1}{R} \, \delta v^{\prime} - \left[\frac{1}{R^2} + k^2 \, N^2 \right] \delta v = C_2 \, I_1(kR) \,, \tag{A.9}$$

which is now a non-homogeneous modified Bessel equation of order one. For any non-homogeneous differential equation, there exists the homogeneous and the particular solutions. Here, we seek $\delta v = \delta v_h + \delta v_p$. The homogeneous part reads

$$\delta v_{\rm h} = C_1 I_1(kNR) \,, \tag{A.10}$$

where, similar to what was done previously, the coefficient of the second term $K_1(kNR)$ has been set to zero because of the boundary conditions of the problem, and A is an arbitrary coefficient. On the other hand, the particular solution

is given by

$$\delta v_{\rm p} = K_1(kNR) \int_R^{R_0} \frac{C_2 I_1(ks) I_1(kNs)}{W(kNs)} ds - I_1(kNR) \int_R^{R_0} \frac{C_2 I_1(ks) K_1(kNs)}{W(kNs)} ds, \tag{A.11}$$

where W(kNs) is the Wronskian for the system and is defined as $W(kNs) := I_1(kNs) K'_1(kNs) - I'_1(kNs) K_1(kNs) = -1/kNs$, which means

$$\delta v_{\rm p} = C_2 k N \left[K_1(kNR) \int_R^{R_0} s \, I_1(ks) \, I_1(kNs) \, ds - I_1(kNR) \int_R^{R_0} s \, I_1(ks) \, K_1(kNs) \, ds \right]. \tag{A.12}$$

Recall that the main balance we need to satisfy is Eq. (19), which contains also the derivatives of δv . These can be obtained from the solution (20), such that $\delta v'$ reads

$$\delta v' = C_1 I_1'(kNR) + C_2 k N \left[K_1'(kNR) \int_R^{R_0} s I_1(ks) I_1(kNs) ds - I_1'(kNR) \int_R^{R_0} s I_1(ks) K_1(kNs) ds \right]$$

$$+ C_2 k N \left[K_1(kNR)R I_1(kR) I_1(kNR) - I_1(kNR)R I_1(kR) K_1(kNR) \right]$$

$$= A I_1'(kNR) + C_2 k N \left[K_1'(kNR) \int_R^{R_0} s I_1(ks) I_1(kNs) ds - I_1'(kNR) \int_R^{R_0} s I_1(ks) K_1(kNs) ds \right].$$
(A.13)

Similarly, the second derivative of δv can be found via

$$\delta v'' = C_1 I_1''(kNR) + C_2 k N \left[K_1''(kNR) \int_R^{R_0} s \, I_1(ks) \, I_1(kNs) \, ds - I_1''(kNR) \int_R^{R_0} s \, I_1(ks) \, K_1(kNs) \, ds \right]$$

$$+ C_2 k N R \, I_1(kR) \left[K_1'(kNR) \, I_1(kNR) - I_1'(kNR) \, K_1(kNR) \right],$$
(A.14)

and since

$$\[K_1'(kNR) I_1(kNR) - I_1'(kNR) K_1(kNR) \] = -W(kNR) = \frac{1}{kNR}, \tag{A.15}$$

the second derivative of δv reads

$$\begin{split} \delta v'' &= C_1 \, I_1''(kNR) + C_2 I_1(kR) \\ &+ C_2 \, k^2 \, N^2 \left[\, K_1''(kNR) \, \int_R^{R_0} s \, I_1(ks) \, I_1(kNs) \, ds - I_1''(kNR) \, \int_R^{R_0} s \, I_1(ks) \, K_1(kNs) \, ds \, \right]. \end{split} \tag{A.16}$$

Having found the solution for δv , we return to (19) and solve for the remaining unknown δu . Looking at the second

equation of (19), we can write $\delta u'$ in terms of δv and its derivatives such that

$$\delta u' = -\frac{\left[1 + \omega \lambda^2 \eta^2\right]}{\omega i k \lambda \eta^3} \left[\delta v'' + \frac{\delta v'}{R} - \frac{\delta v}{R^2}\right] - \frac{ik}{\omega \lambda \eta^3} \delta v. \tag{A.17}$$

Differentiating Eq. (A.17) with respect to r we can also obtain the expression for $\delta u''$ which reads

$$\delta u^{\prime\prime} = -\frac{\left[1 + \omega \lambda^2 \eta^2\right]}{\omega i k \lambda \eta^3} \left[\delta v^{\prime\prime\prime} + \frac{\delta v^{\prime\prime}}{R} - \frac{2\delta v^{\prime}}{R^2} + \frac{2\delta v}{R^3}\right] - \frac{i k}{\omega \lambda \eta^3} \delta v^{\prime} \,. \tag{A.18}$$

We now turn to the first equation of the system (19), which allows us to now write δu also in terms of δv and its derivatives using Eq. (A.17) and (A.18), yielding

$$\delta u = \frac{i}{N^2 \omega k^3 \lambda \eta^3} \left[\delta v^{\prime\prime\prime} + \frac{2\delta v^{\prime\prime}}{R} - \frac{\delta v^{\prime}}{R^2} + \frac{\delta v}{R^3} \right] - \frac{\left[1 - \omega^2 \lambda^2 \eta^6 \right] i}{\left[1 + \omega \eta^4 \right] \omega k \lambda \eta^3} \left[\delta v^{\prime} + \frac{\delta v}{R} \right]. \tag{A.19}$$

The solutions to the differential equation (19) can be summarized as follows

$$\begin{split} \delta v &= C_1 \, I_1(kNR) + C_2 \, k \, N \left[\, K_1(kNR) \, \int_R^{R_0} s \, I_1(ks) \, I_1(kNs) \, ds - I_1(kNR) \, \int_R^{R_0} s \, I_1(ks) \, K_1(kNs) \, ds \, \right], \\ \delta v' &= C_1 \, I_1'(kNR) + C_2 \, k \, N \left[\, K_1'(kNR) \, \int_R^{R_0} s \, I_1(ks) \, I_1(kNs) \, ds - I_1'(kNR) \, \int_R^{R_0} s \, I_1(ks) \, K_1(kNs) \, ds \, \right], \\ \delta v'' &= C_1 \, I_1''(kNR) + C_2 \, k \, N \left[\, K_1''(kNR) \, \int_R^{R_0} s \, I_1(ks) \, I_1(kNs) \, ds - I_1''(kNR) \, \int_R^{R_0} s \, I_1(ks) \, K_1(kNs) \, ds \, \right] \\ &+ C_2 \, k \, N \, R \, I_1(kR) \left[\, K_1'(kNR) \, I_1(kNR) - I_1'(kNR) \, K_1(kNR) \, \right], \\ \delta u &= \frac{i}{N^2 \, \omega \, k^3 \, \lambda \, \eta^3} \left[\delta v''' + \frac{2\delta v''}{R} - \frac{\delta v'}{R^2} + \frac{\delta v}{R^3} \, \right] - \frac{[1 - \omega^2 \, \lambda^2 \, \eta^6 \,]i}{[1 + \omega \, \eta^4 \,] \, \omega \, k \, \lambda \, \eta^3} \left[\delta v' + \frac{\delta v}{R} \, \right], \\ \delta u' &= -\frac{\left[1 + \omega \lambda^2 \eta^2 \, \right]}{\omega i k \lambda \eta^3} \left[\delta v''' + \frac{\delta v'}{R} - \frac{\delta v}{R^2} \, \right] - \frac{ik}{\omega \lambda \eta^3} \, \delta v \, , \\ \delta u''' &= -\frac{\left[1 + \omega \lambda^2 \eta^2 \, \right]}{\omega i k \lambda \eta^3} \left[\delta v''' + \frac{\delta v''}{R} - \frac{2\delta v'}{R^2} + \frac{2\delta v}{R^3} \, \right] - \frac{ik}{\omega \lambda \eta^3} \, \delta v' \, . \end{split}$$

References

- [1] A. Javili, A. McBride, P. Steinmann, B. Reddy, Relationships between the admissible range of surface material parameters and stability of linearly elastic bodies, Philosophical Magazine 92 (28-30) (2012) 3540–3563.
- [2] N. Bain, A. Jagota, K. Smith-Mannschott, S. Heyden, R. W. Style, E. R. Dufresne, Surface tension and the strain-dependent topography of soft solids, Phys. Rev. Lett. 127 (2021) 208001. doi:10.1103/PhysRevLett.127.208001.
- [3] E. S. Matsuo, T. Tanaka, Patterns in shrinking gels, Nature 358 (6386) (1992) 482–485.
- [4] B. Barrière, K. Sekimoto, L. Leibler, Peristaltic instability of cylindrical gels, The Journal of Chemical Physics 105 (4) (1996) 1735–1738.
- [5] C. L. Johnson, A. C. Dunn, Composition controls soft hydrogel surface layer dimensions and contact mechanics, Biointerphases 17 (6) (2022) 061002.
- [6] M. Saeedimasine, A. Montanino, S. Kleiven, A. Villa, Role of lipid composition on the structural and mechanical features of axonal membranes: A molecular simulation study, Sci Rep 9 (1) (2019) 8000.
- [7] E. Evans, R. Waugh, L. Melnik, Elastic area compressibility modulus of red cell membrane, Biophysical Journal 16 (6) (1976) 585–595.
- [8] J. Eggers, Nonlinear dynamics and breakup of free-surface flows, Rev. Mod. Phys. 69 (3) (1997) 865–930.
- [9] S. Mora, T. Phou, J.-M. Fromental, L. M. Pismen, Y. Pomeau, Capillarity Driven Instability of a Soft Solid, Phys. Rev. Lett. 105 (21) (2010) 214301.
- [10] F. Vollrath, D. T. Edmonds, Modulation of the mechanical properties of spider silk by coating with water, Nature 340 (6231) (1989) 305–307.
- [11] V. Sahni, D. V. Labhasetwar, A. Dhinojwala, Spider Silk Inspired Functional Microthreads, Langmuir 28 (4) (2012) 2206-2210.
- [12] S. Ochs, R. Jersild, R. Pourmand, C. Potter, The beaded form of myelinated nerve fibers, Neuroscience 61 (2) (1994) 361-372.
- [13] P. Alstrøm, V. M. Eguíluz, M. Colding-Jørgensen, F. Gustafsson, N.-H. Holstein-Rathlou, Instability and "Sausage-String" Appearance in Blood Vessels during High Blood Pressure, Phys. Rev. Lett. 82 (9) (1999) 1995–1998.
- [14] R. Karyappa, T. Ching, M. Hashimoto, Embedded Ink Writing (EIW) of Polysiloxane Inks, ACS Appl. Mater. Interfaces 12 (20) (2020) 23565–23575.
- [15] H. Fong, I. Chun, D. Reneker, Beaded nanofibers formed during electrospinning, Polymer 40 (16) (1999) 4585–4592.
- [16] T. Ghosh, T. Das, R. Purwar, Review of electrospun hydrogel nanofiber system: Synthesis, Properties and Applications, Polymer Engineering & Science 61 (7) (2021) 1887–1911.
- [17] C. Chen, J. Tang, Y. Gu, L. Liu, X. Liu, L. Deng, C. Martins, B. Sarmento, W. Cui, L. Chen, Bioinspired Hydrogel Electrospun Fibers for Spinal Cord Regeneration, Advanced Functional Materials 29 (4) (2019) 1806899.
- [18] Y. Li, J. Wang, Y. Wang, W. Cui, Advanced electrospun hydrogel fibers for wound healing, Composites Part B: Engineering 223 (2021) 109101.
- [19] P. Ciarletta, M. Ben Amar, Peristaltic patterns for swelling and shrinking of soft cylindrical gels, Soft Matter 8 (6) (2012) 1760.
- [20] M. Taffetani, P. Ciarletta, Beading instability in soft cylindrical gels with capillary energy: Weakly non-linear analysis and numerical simulations, Journal of the Mechanics and Physics of Solids 81 (2015) 91–120.
- [21] C. Xuan, J. Biggins, Finite-wavelength surface-tension-driven instabilities in soft solids, including instability in a cylindrical channel through an elastic solid, Phys. Rev. E 94 (2) (2016) 023107.
- [22] Y. Fu, L. Jin, A. Goriely, Necking, beading, and bulging in soft elastic cylinders, Journal of the Mechanics and Physics of Solids 147 (2021) 104250.
- [23] J. D. McGraw, J. Li, D. L. Tran, A.-C. Shi, K. Dalnoki-Veress, Plateau-Rayleigh instability in a torus: Formation and breakup of a polymer ring, Soft Matter 6 (6) (2010) 1258.
- [24] B. Dortdivanlioglu, A. Javili, Plateau rayleigh instability of soft elastic solids. effect of compressibility on pre and post bifurcation behavior, Extreme Mechanics Letters 55 (2022) 101797.
- [25] D. Emery, Elasto-capillary necking, bulging and maxwell states in soft compressible cylinders, International Journal of Non-Linear Mechanics 148 (2023) 104276.
- [26] S. I. Tamim, J. B. Bostwick, Plateau-Rayleigh instability in a soft viscoelastic material, Soft Matter 17 (15) (2021) 4170-4179.
- [27] S. Seifi, H. S. Park, Electro-elastocapillary rayleigh-plateau instability in dielectric elastomer films, Soft Matter 13 (2017) 4305-4310.
- [28] C. Bächer, K. Graessel, S. Gekle, Rayleigh–Plateau instability of anisotropic interfaces. Part 2. Limited instability of elastic interfaces, J. Fluid Mech. 910 (2021) A47.
- [29] Y. Li, Z. Hu, C. Li, New method for measuring poisson's ratio in polymer gels, Journal of Applied Polymer Science 50 (6) (1993) 1107–1111.
- [30] U. Chippada, B. Yurke, N. A. Langrana, Simultaneous determination of young's modulus, shear modulus, and poisson's ratio of soft hydrogels, Journal of Materials Research 25 (3) (2010) 545–555.
- [31] J. Cappello, V. d' Herbemont, A. Lindner, O. du Roure, Microfluidic In-Situ Measurement of Poisson's Ratio of Hydrogels, Micromachines (Basel) 11 (3) (2020) 318. arXiv:32204340.
- [32] R. Moran, J. H. Smith, J. J. García, Fitted hyperelastic parameters for Human brain tissue from reported tension, compression, and shear tests, Journal of Biomechanics 47 (15) (2014) 3762–3766.
- [33] A. Wahlsten, M. Pensalfini, A. Stracuzzi, G. Restivo, R. Hopf, E. Mazza, On the compressibility and poroelasticity of human and murine skin, Biomech Model Mechanobiol 18 (4) (2019) 1079–1093.
- [34] L. Scriven, Dynamics of a fluid interface Equation of motion for Newtonian surface fluids, Chemical Engineering Science 12 (2) (1960) 98–108.
- [35] M. E. Gurtin, A. Ian Murdoch, A continuum theory of elastic material surfaces, Archive for Rational Mechanics and Analysis 57 (4) (1975) 291–323.
- [36] H. Duan, J. Wang, Z. Huang, B. Karihaloo, Size-dependent effective elastic constants of solids containing nano-inhomogeneities with interface stress, Journal of the Mechanics and Physics of Solids 53 (7) (2005) 1574–1596.
- [37] J. He, C. M. Lilley, Surface Effect on the Elastic Behavior of Static Bending Nanowires, Nano Lett. 8 (7) (2008) 1798-1802.
- [38] R. C. Cammarata, Surface and interface stress effects in thin films, Progress in Surface Science 46 (1) (1994) 1–38.
- [39] R. E. Miller, V. B. Shenoy, Size-dependent elastic properties of nanosized structural elements, Nanotechnology 11 (3) (2000) 139–147.

- [40] Z. P. Huang, J. Wang, A theory of hyperelasticity of multi-phase media with surface/interface energy effect, Acta Mechanica 182 (3-4) (2006) 195–210.
- [41] Z.-Q. Wang, Y.-P. Zhao, Z.-P. Huang, The effects of surface tension on the elastic properties of nano structures, International Journal of Engineering Science 48 (2) (2010) 140–150.
- [42] A. Javili, A. McBride, P. Steinmann, B. D. Reddy, A unified computational framework for bulk and surface elasticity theory: A curvilinear-coordinate-based finite element methodology, Comput Mech 54 (3) (2014) 745–762.
- [43] M. R. Zafar, S. Basu, Calibrating surface hyperelastic constitutive models in soft solids, Phys. Rev. E 103 (6) (2021) 063003.
- [44] S. Heyden, P. M. Vlahovska, E. R. Dufresne, A robust method for quantification of surface elasticity in soft solids, Journal of the Mechanics and Physics of Solids 161 (2022) 104786.
- [45] H. Duan, J. Wang, B. Karihaloo, Theory of Elasticity at the Nanoscale, in: Advances in Applied Mechanics, Vol. 42, Elsevier, 2009, pp. 1–68.
- [46] A. Javili, A. Mcbride, P. Steinmann, Thermomechanics of solids with lower-dimensional energetics: On the importance of surface, interface, and curve structures at the nanoscale. A unifying review, Appl. Mech. Rev. 65 (2013) 010802.
- [47] A. Javili, P. Steinmann, On thermomechanical solids with boundary structures, International Journal of Solids and Structures 47 (24) (2010) 3245–3253. doi:https://doi.org/10.1016/j.ijsolstr.2010.08.009.
- [48] R. W. Ogden, Large deformation isotropic elasticity on the correlation of theory and experiment for incompressible rubberlike solids, Proc. R. Soc. Lond. A 328 (1972) 567–583.
- [49] Z. Liu, A. Jagota, C.-Y. Hui, Modeling of surface mechanical behaviors of soft elastic solids: Theory and examples, Soft Matter 16 (29) (2020) 6875–6889.
- [50] A. D. Bakiler, A. Javili, A Different Catch for Poisson, Springer International Publishing, Cham, 2022, pp. 3-23.
- [51] A. Javili, B. Dortdivanlioglu, A novel constitutive model for surface elasticity at finite strains suitable across compressibility spectrum, European Journal of Mechanics A/Solids 100 (2023) 104981. doi:10.1016/j.euromechsol.2023.104981.
- [52] D. J. Steigmann, R. W. Ogden, Elastic surface-substrate interactions, Proc. R. Soc. A 455 (1999) 437-474.
- [53] B. Dortdivanlioglu, A. Javili, Boundary viscoelasticity theory at finite deformations and computational implementation using isogeometric analysis, Computer Methods in Applied Mechanics and Engineering 374 (2021) 113579.
- [54] K. Paul, R. A. Sauer, An isogeometric finite element formulation for boundary and shell viscoelasticity based on a multiplicative surface deformation split, International Journal for Numerical Methods in Engineering 123 (22) (2022) 5570–5617.
- [55] A. Rastogi, B. Dortdivanlioglu, Modeling curvature-resisting material surfaces with isogeometric analysis, Computer Methods in Applied Mechanics and Engineering 401 (2022) 115649. doi:https://doi.org/10.1016/j.cma.2022.115649.